

PARAMETRIC OPTIMIZATION AND RANKING ANALYSIS OF AA2024–Al₂O₃/AlN ALLOY COMPOSITES FABRICATED VIA STIR CASTING ROUTE UNDER DRY SLIDING WEAR INVESTIGATION

Mukesh Kumar, Ravi Kumar and Sourabh Bhaskar

Mechanical Engineering Department, Malaviya National Institute of Technology, Jaipur, Rajasthan 302017, India

Ashiwani Kumar

Mechanical Engineering Department, Feroze Gandhi Institute of Engineering & Technology, Raebareli, U.P. 229316, India

Copyright © 2023 American Foundry Society
<https://doi.org/10.1007/s40962-023-01053-2>

Abstract

In this investigation, aluminum alloy (AA2024) composite reinforced with ceramic particulates, namely alumina (Al₂O₃) and aluminum nitride (AlN), were designed and fabricated through a semi-automatic stir casting route. The ceramics are added complementary (0–4 wt% @ step of 1%), resulting in five composite specimens, namely ON04, ON13, ON22, ON31, and ON40. The composite specimens are then analyzed for their densities, mechanical, and tribological behavior (steady-state sliding wear analysis), adopting ASTM standards. The Taguchi design of experiment technique was adopted for planning test preliminaries and input sliding wear operating parameters (like sliding velocity, sliding distance, normal load, composition, and environment temperature) optimization using ANOVA. Worn surface morphology studies were reported using a scanning electron microscope (SEM) along with energy-dispersive X-ray spectroscopy (EDS) to understand prevalent wear mechanisms in real time. Additionally, a decision-making technique such as the preference selection

index (PSI) system was used to analyze the alloy composites ranking. The theoretical densities vary 2.784–2.798 g/cc, while actual densities vary 2.539–2.546 g/cc, and voids fraction vary within the 0.5–9.3 % range. The hardness varies 71.6–85.4 HRB, impact strength varies 54–170 J, and tensile strength varies 190–265 MPa. The ranking orders of the significance of input operating factors are environment temperature > normal load > sliding velocity > reinforcement content > sliding distance. It has been found that the alloy composite sample ON22 with an equal presence of both ceramics exhibits overall optimum mechanical properties as well as superior steady-state behavior, which was consistent with the results of the PSI ranking method.

Keywords: AA2024, alumina, aluminium nitride, alloy composites, sliding wear, Taguchi method, preference selection index (PSI)

Introduction

In comparison with other wrought aluminum alloys, AA2024 was found to have good machining, mechanical, and tribological properties. Wrought aluminum alloys reinforced with ceramic particulates have higher stiffness and mechanical properties, making them suitable for structural/mechanical/tribological components in automobiles, aerospace, machinery, marine, and other industries.¹ Numerous research worldwide has been reported in this

direction. A few findings are reported here: Bai et al.² investigated the wear performance of AA2024 –SiC(15 vol.%) - Mo powder (15 vol.%) and found it to have superior anti-wear properties to alloys. Kumar et al.³ investigated the sliding wear and mechanical behavior of Si₃N₄, AlN and ZrB₂-reinforced AA2618 matrix composites under varying reinforcement (0–8 wt%) and applied load test conditions. They found that increasing the reinforcement content increased mechanical properties while decreasing the wear rate and friction coefficient. The wear rate increased, and the friction coefficient decreased marginally with increasing load. Baradeswaran et al.⁴ examined the wear behavior and mechanical properties of

AA7075/Al₂O₃ (2, 4, 6, and 8 wt%) / graphite (5 wt%) hybrid composites. They found tensile strength, flexural strength, hardness, compression strength, and coefficient of friction increase with particulate content. Incorporation of graphite reduced wear in the composites. Kandpal et al.⁵ observed an increase in hardness and a decrease in ductility with increasing Al₂O₃ content in AA6061/Al₂O₃ composite system. Hong et al.⁶ examined the clustering effect on the mechanical properties of AA2024-SiC (3, 5, 7, or 10 vol.%) alloy composites. They observed that the strength of composites generally increased with the increasing volume fraction of the reinforcements. The optimum values appeared to be 5–7 vol.%, with a cluster volume of about 15–20%. Guo-qing et al.⁷ investigated the aging and thermal expansion behavior of the Si₃N₄/AA2024 composite. They found that aging-treated composites exhibit the best dimensional stability owing to low internal stress and strong pinning effect on dislocations from finely dispersed precipitates and high-density tangled dislocations. Abhijit et al.⁸ observed enhancement of microhardness and wear characteristics of tungsten carbide-reinforced AA2024 alloy composites. Pournaderi et al.⁹ studied sliding wear characteristics of AA6061–Al₂O₃ (15–40 vol.%) of size (37–276 μm). The wear behavior of coarse alumina reinforced was found to be better than fine, in general. The 20 vol.% of Al₂O₃ with a mean size of 150 μm gives optimal results. Akhlaghi et al.¹⁰ studied the dry and oil-impregnated sliding wear behavior of AA2024-graphite (5–20%). They found that the coefficient of friction for both dry and oil-impregnated sliding conditions was decreased with an increase in Gr content and exhibited superior wear properties over the base alloy. Hosseini et al.¹¹ studied the wear behavior of AA6061/Al₂O₃ (0–5 vol.%) composites. They found 3 vol.% Al₂O₃ reinforcement exhibits maximum hardness and optimum wear rate, beyond which hardness decreases with sharp wear rate. Selvam et al.¹² examined the mechanical properties of AA6061-TiB₂ + Al₂O₃ (0, 5, 10, and 15 wt.%) alloy composites and reported the highest magnitudes at 15 wt.%. Jacob et al.¹³ observed enhancement of microhardness and wear performance in aluminum alloys reinforced with graphite and Al₂O₃ particulates. Sharma et al.¹⁴ studied the microstructural, physical, and mechanical characteristics of AA6082–Si₃N₄ (0, 3, 6, 9, and 12 wt%) alloy composites. They observed the presence of Si₃N₄ particulates in the microstructural examination. The density, voids content, hardness, and tensile strength increased with reinforcement while ductility decreased. Umanath et al.¹⁵ investigated dry sliding wear characteristics of hybrid Al alloy composite filled

with 5 and 15 wt.% of (SiC + Al₂O₃) particulates. They observed lower wear loss for a large amount of filler particles, smaller applied load, minimum rotational speed, and higher hardness of the counter surface. Devaraju et al.¹⁶ investigated AA6061-T6 alloy composite reinforced with graphite, SiC, and Al₂O₃ particulates. The hardness was significantly enhanced as compared to the base alloy. The presence of SiC with Gr in the alloy has shown more wear resistance than the presence of SiC with Al₂O₃ particulates. Dharmalingam et al.¹⁷ investigated the sliding wear characteristics of Al–Si–10Mg alloy reinforced with 2 and 4 wt% MoS₂, 5 wt% Al₂O₃ particulates. They observed a minimum wear rate for an applied normal load of 30 N, sliding speed of 4 m/s, and at 4 wt%. MoS₂. Kok¹⁸ observed significant improvement in the abrasive wear characteristics of AA2024–30 wt.% Al₂O₃ alloy composites. Ozdemir et al.¹⁹ investigated the mechanical properties of AA2017–SiC (5 vol.%)–Al₂O₃ (15 vol.%) alloy composites. They observed higher UTS for 15 vol.% fine SiC than other compositions.

In this investigation, aluminum alloy (AA2024) composites reinforced with a complementary combination of ceramic particulates, namely alumina (Al₂O₃) and aluminum-nitride (AlN) with graphite as additives, were fabricated through a semi-automatic stir casting route. This research study aims to improve the overall mechanical properties of the alloy so that its structural and tribological functionality can be enhanced. Furthermore, the Taguchi design of experiment technique was used to optimize parameter values using ANOVA, and a decision-making tool called the preference selection index (PSI) method was used to rank alloy composites.

Experimental Details and Methodology

Materials and Fabrication Procedure

Aluminum alloy AA2024 (supplied by Vijay Prakash Aero-marine Metals Pvt. Ltd., New Delhi, India) having copper (4.3–4.5%), manganese (0.5–0.6%), magnesium (1.3–1.5%), and zinc, nickel, chromium, lead, bismuth (<0.5%) has been used as base alloy metal matrix²⁰ as confirmed by Batra Metallurgical & Spectro Station, New Delhi, is shown in Table 1. The master batch consisting of a constant fraction of alloy matrix and graphite additive as a solid lubricant (2 wt.%, supplied by Central Drug House Private Limited, New Delhi; particle size of 99 μm) was

Table 1. The Compositional Analysis of AA2024 Alloy²⁰

Element:	Al	Cr	Cu	Fe	Mg	Mn	Si	Ti	Zn	Pb
Content (wt%):	Bal	0.02	4.11	0.21	1.48	0.55	0.33	0.02	0.13	0.01

Table 2. Materials Properties Under Investigation^{21,22}

Properties Materials	Melting point (°C)	Density (g/cc)	Tensile strength (MPa)	Flexural strength (MPa)	Young's modulus (GPa)	Thermal conductivity (W/mK)
AA2024	500	2.78	185	237	70-80	193
Graphite	3600	2.28	115	50	4.8	24
Aluminum Nitride	2200	3.26	197-270	320	330	285
Aluminum Oxide	2702	3.82	260-300	310-379	393	35

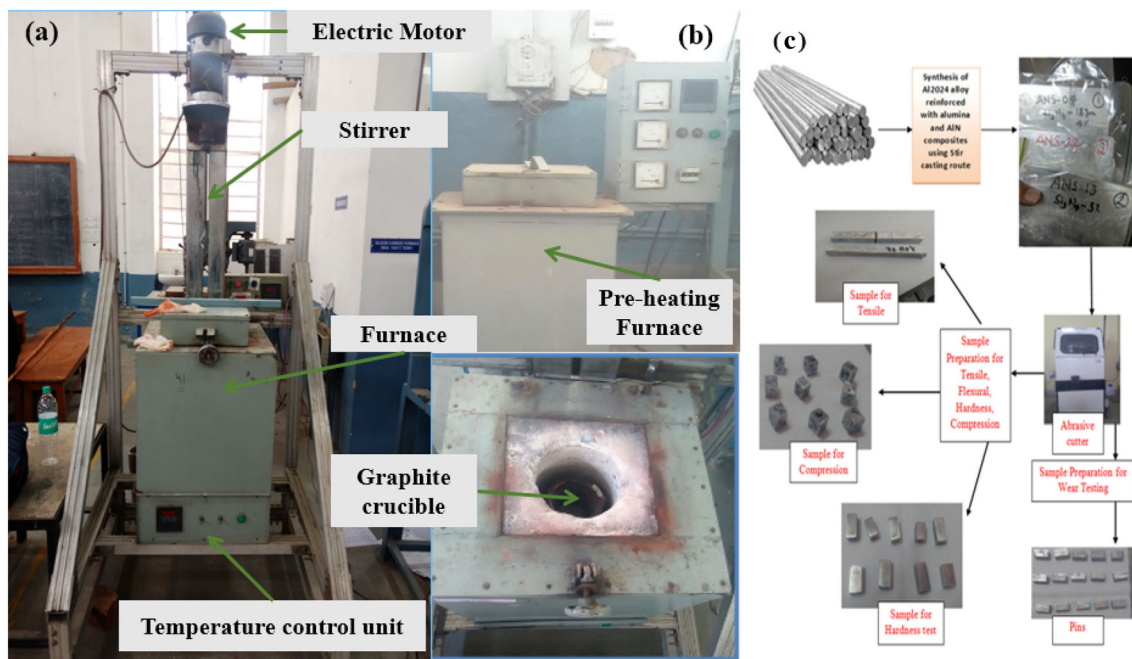


Figure 1. (a) Semi-automatic Stir casting, (b) Pre-heating furnace, (c) Sample preparation.

reinforced with a complementary combination (0-4 wt.% @ step of 1%) of alumina (locally supplied by ASES Chemical Works, Jodhpur, particle size of 30–80 μm; 99% purity) and aluminum nitride particulates (as supplied by Triveni Chemicals, Gujarat; particle size of 30-80 μm; 99% purity); thereby, five compositions were developed, namely ON04, ON13, ON22, ON31, ON40 (where the first letter signifies alumina while second letter for aluminum nitride, first digit proportion of alumina similarly second digit for aluminum nitride). The properties of materials are shown in Table 2. A semi-automatic stir-casting (Figure 1a) technique was used to fabricate the designed formulation. The cleaned small cut pieces of alloy matrix were melted in electrical resistance furnaces at ~720°C using a graphite crucible. After that, magnesium powder of ~ 2 wt% was added to enhance the wettability of pre-heated (at ~700°C for 3 hrs) (Figure 1b) reinforcements with alloy matrix. To improve the uniform distribution of the reinforcing phase in the alloy matrix, an automatic stirrer (made of steel) of speed = 450 rpm; time = 10 min. was used. The mixture was held at the same temperature for ~ 5–10 min. to

maintain consistent melt viscosity and ensure complete phase change. After this, the mixture was stirred for a while to mix any segregation and easily poured into a permanent cast-iron mold (size 150 mm × 140 mm × 10 mm); after that, the molten mixture was allowed to solidify in the open air at room temperature. After this, specimen samples were prepared for various characterizations following prevalent standards using an in-house abrasive cutting machine and polished using 1000 mesh emery paper simultaneously (Figure 1c).

Density and Mechanical Characterization

The theoretical density (ρ_{ct}) of the investigated alloy composites was calculated using Eqn. 1, as proposed by Aggarwal and Broutman:²³

$$\frac{1}{\frac{W_{Al2024}}{\rho_{Al2024}} + \frac{W_{Al_2O_3}}{\rho_{Al_2O_3}} + \frac{W_{AlN}}{\rho_{AlN}} + \frac{W_{Gr}}{\rho_{Gr}}} \quad \text{Eqn. 1}$$

Table 3. Experiment Parameters with Different Levels

Factor	Level					Unit
	I	II	III	IV	V	
Sliding velocity	0.565	1.132	1.696	2.262	2.825	m/s
Sliding distance	678	1357	2035	2714	3392	m
Reinforcement Composition	ON04	ON13	ON22	ON31	ON40	ON series (wt%)
Normal load	10	20	30	40	50	N
Environment temperature	30	35	40	45	50	°C

where w and ρ represent the weight fraction and density, respectively. The specimens' actual densities (ρ_{ce}) were obtained experimentally by a simple water immersion technique following the Archimedes principle (ASTM D792). The presence of voids (V_c) in the composite samples was determined using the following Eqn. 2:²⁴

$$V_c = \frac{\rho_{ct} - \rho_{ce}}{\rho_{ct}} \quad \text{Eqn. 2}$$

The tensile strength (specimen dimension of 140 mm × 12 mm × 10 mm; the crosshead speed of 2 mm/min.; span length of 65 mm as per ASTM D 3039-76²⁵ as well as flexural strength (specimen dimension of 127 mm × 12.5 mm × 4 mm; the crosshead speed of 2 mm/min.; span length of 70 mm as per ASTM D 2344-84²⁵ were evaluated using UTM of Instron company.

For impact strength (J) measurement, the Charpy V-notch test (ASTM D-256) was performed on the Charpy Impact tester machine.²⁵ The sample dimension was 55 mm × 10 mm × 10 mm (notch at 45°; 2.5 mm depth). Rockwell hardness test method using B-scale on Krystal Elmec Rockwell hardness tester, meant for aluminum alloys as per ASTM E18,²⁵ was adopted for hardness measurement.

Sliding Wear Tribometer and Surface Morphology Studies

DUCOM-supplied pin-on-disk tribometer was used to simulate sliding wear experimental test runs following ASTM G99, using cylindrical pin-shaped specimens of dimensions 25 mm (height) × 10 mm (diameter). The hardened ground steel (EN-31) disk of hardness 62 HRC and 0.6 μRa surface roughness was used as a counter-body. Further, precision electronic balance with an accuracy of ± 1 mg was used to ascertain material loss of pin before and after the test runs. The tribometer uses WinDucom 2010-V07 software on a window operating system for proper machine control as per input parameter level, data acquisition, and post-processing calculations. For the computation of specific wear rate (mm³/Nm), Eqn. 3 may be used:

$$W_s = \frac{\Delta m}{\rho t V_s F} \left(\frac{\text{mm}^3}{\text{Nm}} \right) \quad \text{Eqn. 3}$$

where Δm refers to mass loss during a test run (g), ρ refers to the density of the composite (g/mm^3), t refers to test duration (s), V_s refers to sliding velocity (m/s), and F refers to average normal load (N).

The prevalent wear mechanisms of the alloy composites during sliding wear may be studied with worn surface micrographs taken with the help of a scanning electron microscope (SEM) equipped with energy-dispersive X-ray spectroscopy (EDS) that reveals elemental composition and its dispersion on the worn surface; the equipment was supplied by FEI.

Taguchi Optimization Method

Taguchi's design of experiment methodology was adopted to (i) simulate experimental runs, (ii) identification of input control factors, as shown in Table 3, that control the output response performance, i.e., specific wear rate of alloy composites, (iii) investigate the order of input operating factors that actively monitors response performance of the alloy composites. L₂₅ orthogonal array was adopted for designing experimental trials and corresponding S/N ratio and analysis of variance (ANOVA) was computed for analysis as per methodology. To implement the methodology, MINITAB 17 software was used. For the objective of minimum specific wear rate of alloy composites, the smaller-the-better S/N ratio characteristic was adopted as per Eqn. 4:²⁶

$$\begin{aligned} \text{Smaller – the – better characteristic : } & \frac{S}{N} \\ & = -10 \log \frac{1}{n} \sum y^2 \end{aligned} \quad \text{Eqn. 4}$$

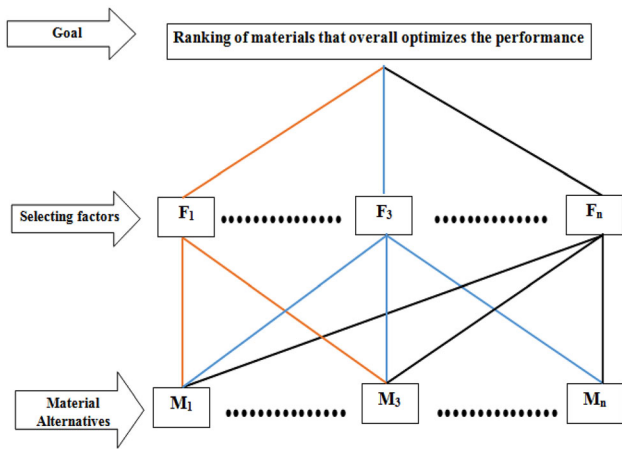


Figure 2. The hierarchy chart of the decision-making problem.

where ‘n’ refers to the number of trials, and y refers to the observed data.

Preference Selection Index Method Procedure

The procedure of the PSI algorithm comprises:²⁷⁻³³

Step 1: Formulation of the decision problem: It includes input data or information to PSI like ascertaining material alternatives, selecting factors, and its measures specific to the application. All these enable goal identification or finalization. The general hierarchy structure related to the investigating problem is represented in Figure 2.

Step 2: Determining decision matrix: The multi-alternative (say *m*-alternatives) and multi-criteria (say *n*-criteria) of the stated problem can be expressed in terms of decision matrix (say matrix *D* of *m* × *n* order):

$$D_{m \times n} = \begin{matrix} & C_1 & C_2 & \cdots & C_n \\ A_1 & \begin{bmatrix} p_{11} & p_{12} & \cdots & p_{1n} \end{bmatrix} \\ A_2 & \begin{bmatrix} p_{21} & p_{22} & \cdots & p_{2n} \end{bmatrix} \\ \vdots & \begin{bmatrix} \vdots & \vdots & \ddots & \vdots \end{bmatrix} \\ A_m & \begin{bmatrix} p_{m1} & p_{m2} & \cdots & p_{mn} \end{bmatrix} \end{matrix}$$

where C_1, C_2, \dots, C_n are the *n*-criteria and

A_1, A_2, \dots, A_m are the *m*-alternatives

The element p_{ij} is the performance value of the i^{th} alternative (A_i) with respect to the j^{th} attribute (C_j) where $i = 1, 2, \dots, m$, and $j = 1, 2, \dots, n$.

Step 3: Computation of Normalized matrix: The data of the above matrix are normalized using criteria (i) if *larger-the-better* was the expectancy, then the original attribute performance normalized as $R_{ij} = \frac{x_{ij}}{x_{j, \max}}$; (ii) If *smaller-the-better* was the expectancy, then the original attribute performance

normalized as $R_{ij} = \frac{x_j^{\min}}{x_{ij}}$, where x_{ij} is the attribute measures ($i = 1, 2, 3, \dots, m$ and $j = 1, 2, 3, \dots, n$).

The normalization process transformed the decisive data into a range of 0 to 1. This is necessary as it transformed different performance ratings with different data measurement units into a compatible one, whereby all the criteria are measured dimensionless. Hence, facilitate inter-attribute comparisons.

Step 4: Determining preference variation value (PV_j): The computed normalized matrix R_{ij} , further be used to find preference variation value (PV_j) for each criterion using the sample variance concept expressed as:

$$PV_j = \sum_{i=1}^N (R_{ij} - \bar{R}_j)^2$$

where \bar{R}_j is the mean of the normalized value of criteria j , i.e., $\bar{R}_j = \frac{1}{n} \sum_{i=1}^N R_{ij}$

Step 5: Determining overall preference value (ψ_j): The overall preference value (ψ_j) of each criterion is computed using the:

$$\Psi_j = \frac{\Phi_j}{\sum_{j=1}^n \Phi_j}$$

where, $\Phi_j = 1 - \sum PV_j$, is the deviation in preference value of each criterion. For consistency, the sum of the overall preference value for all the criteria should be unity, i.e., $\sum \psi_j = 1$.

Step 6: Determination of preference selection index (I_i): The preference selection index (I_i) for each alternative is computed using the following:

$$I_i = \sum_{j=1}^n (R_{ij} \times \Psi_j)$$

Step 7: The computed values of the preference selection index (I_i), is used further for ranking of alternatives in descending order i.e., highest-to-lowest.

Results and Discussions

Density and Mechanical Performance

The evaluated mechanical strength, experimental density, theoretical density, and voids fraction of the alloy composites are listed in Table 4 and plotted in Figures 3, 4.

Density and Voids Content

The ambient, experimental densities of the investigated alloy composites remain within 2.539-2.546 g/cc; while

Table 4. Density and Mechanical Properties

Characteristics: Composites	ON04	ON13	ON22	ON31	ON40
Experimental density (g/cc)	2.546	2.605	2.776	2.562	2.539
Standard deviation (density)	0.014	0.084	0.072	0.208	0.151
Theoretical density (g/cc)	2.784	2.788	2.791	2.794	2.798
Voids content (%)	8.5	6.6	0.5	8.3	9.3
Ultimate tensile strength (MPa)	206	245	265	213	190
Standard deviation (tensile strength)	4.355	4.603	3.092	1.572	3.109
Flexural strength (MPa)	258.48	272.91	364.03	296.98	267.99
Standard deviation (flexural strength)	3.790	3.606	3.403	4.388	2.101
Hardness (HRB)	71.6	72.6	78.2	79.0	85.4
Standard deviation (hardness)	1.486	1.184	1.023	0.980	1.500
Impact strength (J)	54	80	170	66	48
Standard deviation (impact strength)	4.359	3.606	3.606	3.000	3.953

theoretical densities remain within 2.784-2.798 g/cc and voids fraction within the 0.5-9.3% range (Table 4; Figure 3). The theoretical densities show an increasing trend and seem to dominate the experimental densities across the formulation. This is obvious due to the ideal state assumption within the material, i.e., there is a perfect state having no imperfections. Any deviation from this perfect state like improper wettability, mixing, or adhesion may cause a decrement in the magnitude of density (i.e., experimental densities) and leads to the formation of voids.²⁵ The actual densities seem to follow the order: ON22 > ON13 > ON31 > ON40 > ON04, while voids fraction follows the order: ON40 > ON04 > ON31 > ON13 > ON22. Thus, it may be inferred that the synergistic presence of both ceramics in equal proportion leads to better interfacial adhesion between matrix reinforcement relative to other alloy composites.

Consequently, experimental density approaches theoretical density, leading to the least voids content. The alloy composites ON13/ON31 show the next order according to the presence of proportionate ceramic viz. (alumina ~3.82 g/cc; AlN ~ 3.26 g/cc). The higher voids content leads to poor quality products as physical, tribological, and machining properties are badly affected.²⁵ Similar observations are reported by Kumar et al.¹

Mechanical Strength Properties

The rockwell hardness (HRB) measurement was carried out for the alloy composite samples. The hardness magnitude of the alloy composites improves across the formulation, owing to the mutual effect of ceramic reinforcement in the base alloy matrix, also due to the incremental presence of alumina harder phase in a complementary combination of aluminum nitride phase. The addition of ceramic particulates was reported to have finer

grain size and uniform dispersion in the base alloy matrix, enhancing the interfacial adhesion between ingredients and making the matrix stiffer against any deformation.³⁴ This promotes the load-bearing resistance of the material. In alloy composites, the reinforcement is supposed to bear the entire deforming load, transferred by the base alloy matrix, thereby preventing pre-mature fracturing of material from the surface. Similar results are discussed by Kok.¹⁸

The impact strength characteristic of the alloy composite follows the order: ON22 (170 J) > ON13 (80 J) > ON31 (66 J) > ON04 (54 J) > ON40 (48 J), as depicted in Figure 4, Table 4. The presence of lowest voids (in the case of ON22) leads to superior interfacial adhesion among reinforcement-matrix systems, together with the generation of finer grain, may lead to strengthening the toughness mechanism that ultimately improves the impact load-bearing capacity of the alloy composites as advocated by Hall-Petch equation,³⁵ Bhaskar et al.²¹ and Kumar et al.²⁴. The same is less pronounced in the case of ON13/ON31 and least with ON04/ON40.

The tensile strength follows the order: ON22 (265 MPa) > ON13 (245 MPa) > ON31 (213 MPa) > ON04 (206 MPa) > ON40 (190 MPa), as depicted in Figure 4, Table 4. The mutual equal presence of ceramic particulates in the alloy matrix leads to minimal voids fraction, strengthening interfacial interactions among ingredients and making efficient load transfer from the matrix to the particulate phase during tensile tests. For other compositions, the characteristics follow the void content. Voids act as a site for stress concentrator-raisers that hinder load transfer mechanisms, lowering the strength under tensile tests.²⁵

The flexural strength follows the order: ON22 (364 MPa) > ON31 (297 MPa) > ON13 (272.9 MPa) > ON40 (267.99 MPa) > ON04 (258.48 MPa) as depicted in Figure 4, Table 4. The characteristics of lower voids fraction of

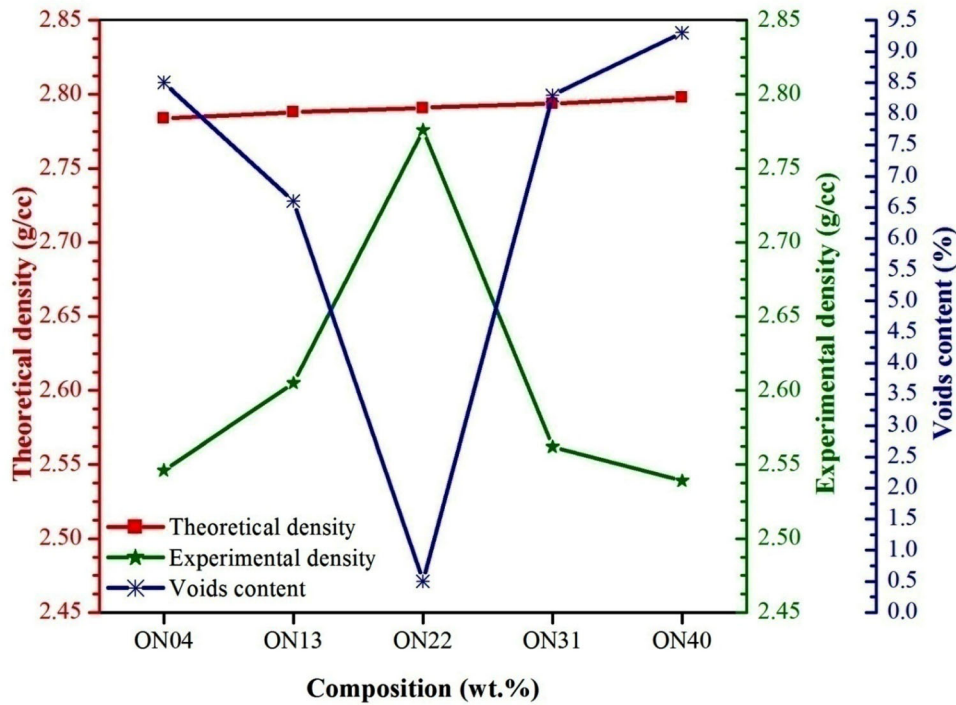


Figure 3. Density and voids content properties.

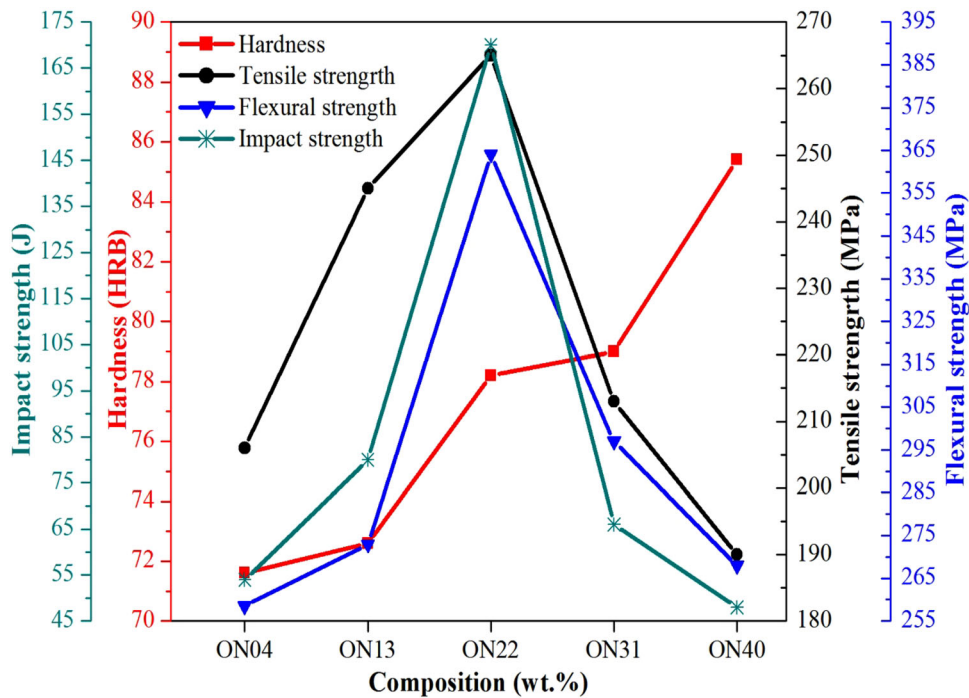


Figure 4. Mechanical strength properties.

ON22 alloy composites makes stiffer matrix-reinforcement interfacial adhesion that enhances lateral strength against any cracking mechanisms and makes an efficient load transfer mechanism. The presence of equal ceramic reinforcement phases might show synergistic roles that give a better matrix-reinforcement interface. In contrast, in other

cases, voids result in stress concentration, builders, and raisers that lead to the specimen's premature failure when subjected to flexural loads.^{36,37}

Table 5. Taguchi Experimental Design Using L₂₅ Orthogonal Array

Sr. No.	Sliding velocity (m/s)	Reinforcement content (%)	Sliding distance (m)	Normal load (N)	Environment temperature (°C)	Sp. Wear rate (mm ³ /Nm)	SNR (dB)
1.	0.565	ON04	678	10	30	0.000637	64
2.	0.565	ON13	1357	20	35	0.0001981	74
3.	0.565	ON22	2035	30	40	0.0002656	72
4.	0.565	ON31	2714	40	45	0.0003455	69
5.	0.565	ON40	3392	50	50	0.0001879	75
6.	1.132	ON04	1357	30	45	0.0002507	72
7.	1.132	ON13	2035	40	50	0.000106	79
8.	1.132	ON22	2714	50	30	0.0000902	81
9.	1.132	ON31	3392	10	35	0.0002014	74
10.	1.132	ON40	678	20	40	0.0001613	76
11.	1.696	ON04	2035	50	35	0.000054	85
12.	1.696	ON13	2714	10	40	0.0000943	81
13.	1.696	ON22	3392	20	45	0.0002389	72
14.	1.696	ON31	678	30	50	0.0001151	79
15.	1.696	ON40	1357	40	30	0.0000929	81
16.	2.262	ON04	2714	20	50	0.0001157	79
17.	2.262	ON13	3392	30	30	0.000066	84
18.	2.262	ON22	678	40	35	0.000063	84
19.	2.262	ON31	1357	50	40	0.0000633	84
20.	2.262	ON40	2035	10	45	0.0007186	63
21.	2.825	ON04	3392	40	40	0.0000666	84
22.	2.825	ON13	678	50	45	0.0002104	74
23.	2.825	ON22	1357	10	50	0.0002442	72
24.	2.825	ON31	2035	20	30	0.0000691	83
25.	2.825	ON40	2714	30	35	0.0002269	73

Parametric Optimization

Taguchi's experimental design (see section "Taguchi optimization method"), having an L₂₅ orthogonal array, was used for sliding wear performance test runs. Table 5 lists the scheme of the design along with experimentally evaluated SWR (using Equation 4) and S/N ratio (using Equation 5). The plot of the main factors for the S/N ratio is depicted in Figure 5. Table 6 lists the order of significance of input operating factors and ANOVA results in Table 7, followed by the confirmation test results in Table 8. MINITAB 17 analytical tools were used for calculations to implement the methodology.

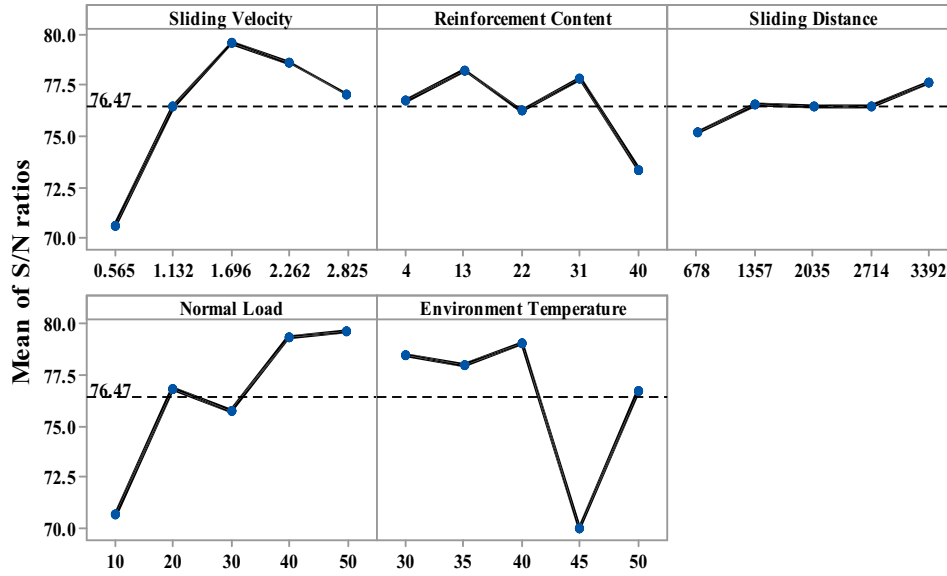
The analysis reveals an average S/N ratio for SWR to be 76.47 dB. The orders of significance (Table 6) of input operating factors are Environment temperature > normal load > Sliding velocity > Reinforcement content > Sliding distance. The factor combination setting A₃B₂C₅D₅E₃ (Figure 5), i.e., sliding velocity = 1.696 m/s, reinforcement content of ON13, sliding distance = 3392 m, normal load = 50 N, and environment temperature = 40°C, found to give optimal SWR of the specimens.

Further, the analysis of variance (ANOVA) tool is used to ascertain the extent of the contribution of operating factors and their significance order on the SWR of alloy composites under investigation quantitatively. Here, the significance level (denoted by 'p') of 5% (i.e., the level of confidence of 95%) is taken. The lower magnitude of 'p' signifies a higher contribution of that factor in the output response. In this sense order of influence of input control factors is environment temperature (P = 29.76%) > normal load (P=28.54%) > sliding velocity (26.23%) > reinforcement content (8.03%) > sliding distance (P=1.55). Thus, the ranking order listed in Table 6 and ANOVA Table 7 are in agreement.

The last step of Taguchi methodology was to perform confirmation tests to validate the conclusion made in the above analysis phase. For this, an arbitrary factor combination says A₄ B₂ C₅ D₄ E₁ would be taken to predict the SWR. The predictive Equation 5 may be used to estimate the S/N ratio for the SWR

Main Effects Plot for S/N ratios

Data Means



Signal-to-noise: Smaller is better

Figure 5. Effect of input operating factors on SWR.

Table 6. Order of Significance of Input Control Factors

Level	Sliding velocity (m/s)	Reinforcement content (%)	Sliding distance (m)	Normal load (N)	Environment temperature(°C)
1.	70.65	76.71	75.22	70.69	78.45
2.	76.43	78.24	76.59	76.86	78.05
3.	79.54	76.22	76.49	75.76	79.07
4.	78.64	77.82	76.45	79.38	70.02
5.	77.08	73.35	77.60	79.66	76.75
Delta	8.89	4.89	2.38	8.96	9.06
Rank	3	4	5	2	1

Table 7. ANOVA Results for Specific Wear Rate

Source	DF	Seq SS	Adj SS	Adj MS	F	P	P(%)
Sliding velocity (m/s)	4	242.02	242.02	60.506	4.46	0.088	26.23
Reinforcement content	4	74.05	74.05	18.513	1.36	0.386	8.03
Sliding distance (m)	4	14.32	14.32	3.579	0.26	0.888	1.55
Normal load (N)	4	263.33	263.33	65.832	4.85	0.078	28.54
Environment temperature (°C)	4	274.55	274.55	68.637	5.05	0.073	29.76
Error	4	54.32	54.32	13.581			
Total	24	922.59					

S (3.685); R-sq (94.11%); R-sq(adj) (64.67%); R-sq(pred)(0.00%)

Table 8. Results of the Confirmation Experiment for SWR

	Optimal control parameter		
	Prediction	Experimental	Error
Level	A ₄ B ₂ C ₅ D ₄ E ₁	A ₄ B ₂ C ₅ D ₄ E ₁	
S/N ratio for SWR (dB)	86.29	83.47	3.38 %

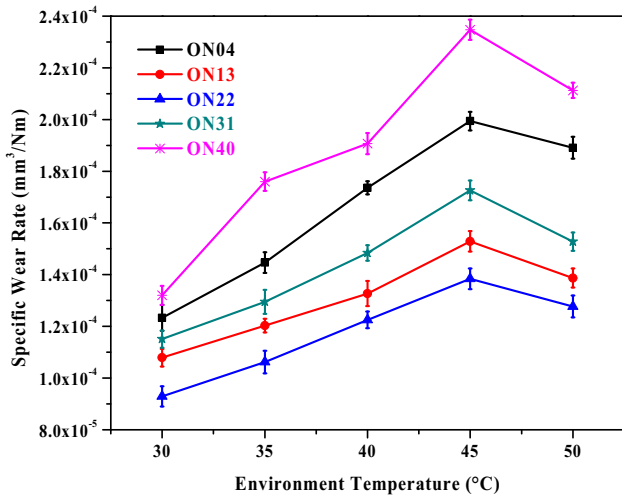


Figure 6. Effect of environmental temperature on the specific wear rate.

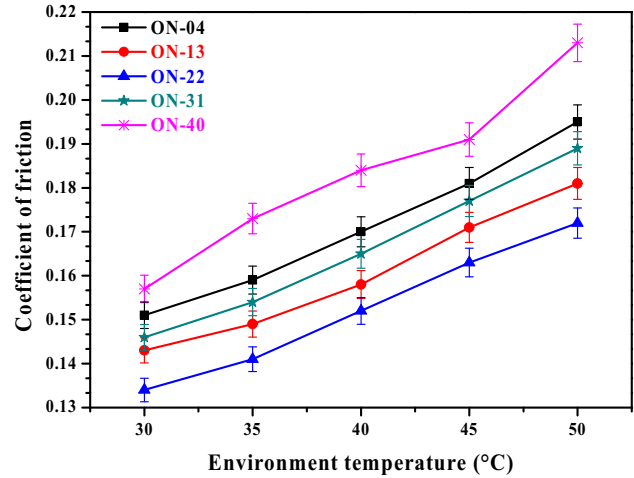


Figure 7. Effect of environmental temperature on the coefficient of friction.

$$\bar{\eta}_1 = \bar{T} + \frac{[\overline{A_4} - \bar{T}]}{4} + \frac{[\overline{B_2} - \bar{T}]}{2} + \frac{[\overline{C_5} - \bar{T}]}{5} + \frac{[\overline{D_4} - \bar{T}]}{4} + \frac{[\overline{E_1} - \bar{T}]}{1}$$

Eqn. 5

where $\bar{\eta}_1$ is the predicted average; \bar{T} is the overall experimental average; $\overline{A_4}, \overline{B_2}, \overline{C_5}, \overline{D_4}$ and $\overline{E_1}$ are the average response for the factors at respective levels. The S/N was found to be $\bar{\eta}_1 = 86.29$ dB using Equation 5. After that, conformational test trials were performed for the factor combinations (A₄ B₂ C₅ D₄ E₁) settings. The obtained results of 83.47 dB were then compared with the predictive result ($\bar{\eta}_1$) (Table 8), and an error of 3.38% was found. More experimental trials may further reduce the computed error. Thus, the model suitably predicts the SWR of the alloy composites with reasonable accuracy.

The significant findings are: (i) with an increase in S/N ratio up to 1.696 m/s and after that, it falls; hence the SWR shows declining rates up to 1.696 m/s, and after that, it increases (ii) as the S/N ratio increases with sliding distance, so the SWR decreases continuously with minimum magnitude at 3392 m (iii) as the S/N ratio increases with normal load and attained maximum magnitude at 50 N, so the SWR decreases with load with minimum magnitude at 50 N (iv) as the S/N ratio shows minimum magnitude at 45 °C, so the SWR shows the maximum value at 45 °C. Thus, the results of the Taguchi design-of-experiment are in-tune with that of steady-state experimental results (see

Figures 6, 7, Section “Effect Of Environment Temperature On Swr/COF”)

Steady State-Specific Wear Rate and Coefficient of Friction Analysis

Effect of Environment Temperature on SWR/COF

The specific wear rate and coefficient of friction of the investigated alloy composites under steady-state conditions of environment temperature (i.e., temperature = 30, 35, 40, 45, 50 °C; sliding velocity = 1.132 m/s; normal load = 20 N; sliding distance = 1357 m) are shown in Figures 6, 7. It is observed that (i) the specific wear rate of the alloy composites increases as the operating temperature increases up to 45°C with an interfacial flash temperature between pin-disk interfaces; thereafter, it suddenly drops irrespective of reinforcement across the formulations. This may be due to the relative softening of interfacial binding between matrix reinforcement at higher temperatures that might accelerate the particulate detachment in the form of wear debris. These hard debris particulates promote a three-body abrasive wear mechanism across the pin-disk interface and further accelerate the wear rates.³⁸ (ii) At any specific operating temperature, the order of wear performance seen across the entire range is ON40 > ON04 >

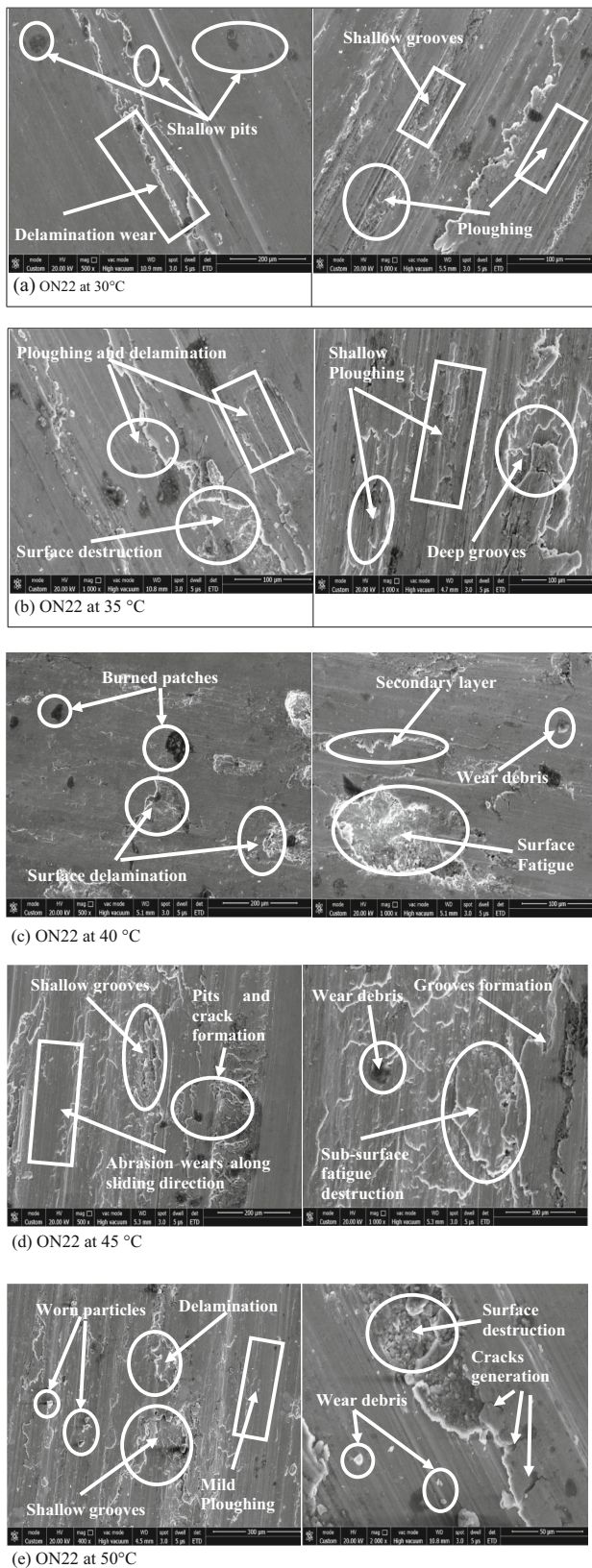


Figure 8. Surface micrographs of ON22 alloy composites.

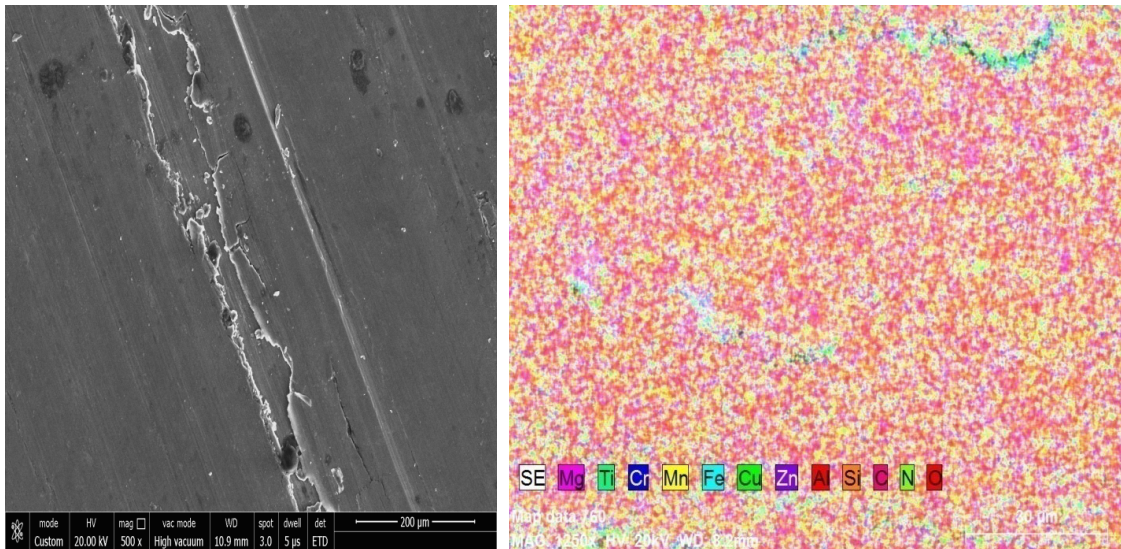
ON31 > ON13 > ON22. This is possibly due to the voids fraction affecting interfacial adhesion and mechanical

properties (see section “Density and Mechanical Performance”). The alloy composites with either ceramic particulate or unequal complementary presence have higher voids fraction and lower mechanical properties than alloy composites of equal ceramic presence in a base alloy matrix. Thus, later formulation enables an intact hold of ingredients even at higher temperatures, hence improving specific wear rate.

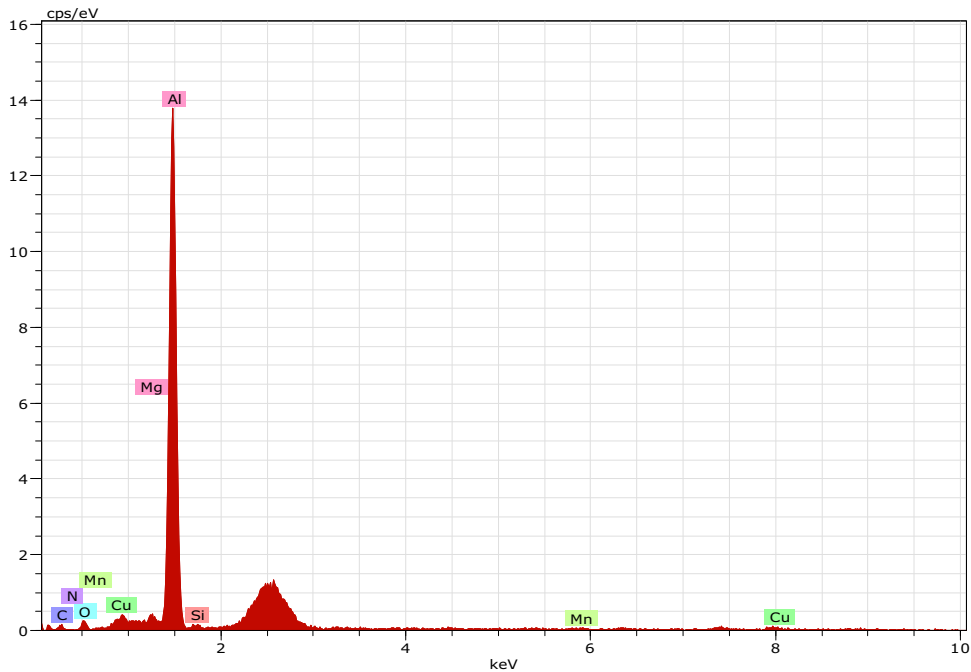
From Figure 7, (i) the coefficient of friction was observed to have an increasing trend with the operating environment temperature range regardless of reinforcement proportions in the alloy composites. This may be possibly due to the fact that environment temperature, together with an instant flash temperature between pin-disk interfaces, promotes the mechanism of formation – distortion – decimation - reorganization of tribo-layer containing ceramic particulates that further accelerates the frictional forces at contact asperities that seems to improve the magnitude of the coefficient of friction. (ii) At any specific operating temperature, the order of coefficient of friction seen across the entire range is ON40 > ON04 > ON31 > ON13 > ON22. This is the mutual contribution of the physical and mechanical performance of the alloy composite. The alloy composite having the equal presence of ceramic particulates has enhanced mechanical properties; hence its tendency to liberate wear debris particulates is relatively lesser than other alloy composites having either or unequal ceramic reinforcements; hence it has a relatively thinner tribo-layer that generates relatively lesser wear debris hence shows a lesser tendency to have a higher magnitude of the coefficient. Similar results are reported in the literature.³⁹

Wear Surface Morphology Analysis

Figure 8 shows the worn surface morphology studies using scanning electron microscopy so as to understand the wear mechanisms responsible for surface damage of the investigated alloy composites under the steady-state condition of environment temperature (as discussed in section “Parametric optimization”), as its contribution is significant (Table 6). The mechanical and physical characteristics (see Figures 3, 4) of ON22 alloy composites show relatively better performance than others; hence there is an indication of a better synergistic combination between ceramic reinforcements and alloy matrix, i.e., superior interfacial adhesion or bonding between constituents. Consequently, the mechanism of external load transfer to reinforcement via matrix is more efficient. This phenomenon decreases the tendency of reinforcement detachment, debris formation, and, indirectly, the rate of sliding wear. Figure 8a shows sliding wear surface damage of alloy composite at 30 °C. A thin tribo-layer due to solid self-lubricant graphite over the damaged surface, combined with the presence of shallow pits, grooves, and delaminated surfaces with



(a1): SEM area form where mapping data has been collected (a2): EDAX mapping of the elements present in ON04 alloy composite



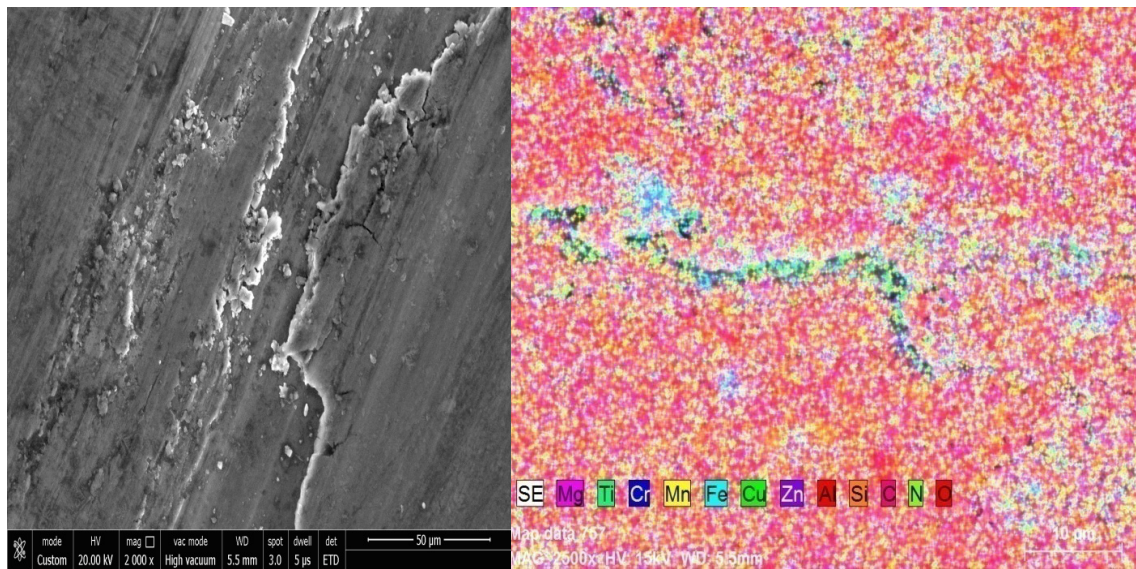
(a3): EDAX spectra showing elements present in ON04 alloy composite
(a) ON04alloy composite

Figure 9. EDAX plot of hybrid alloy composites.

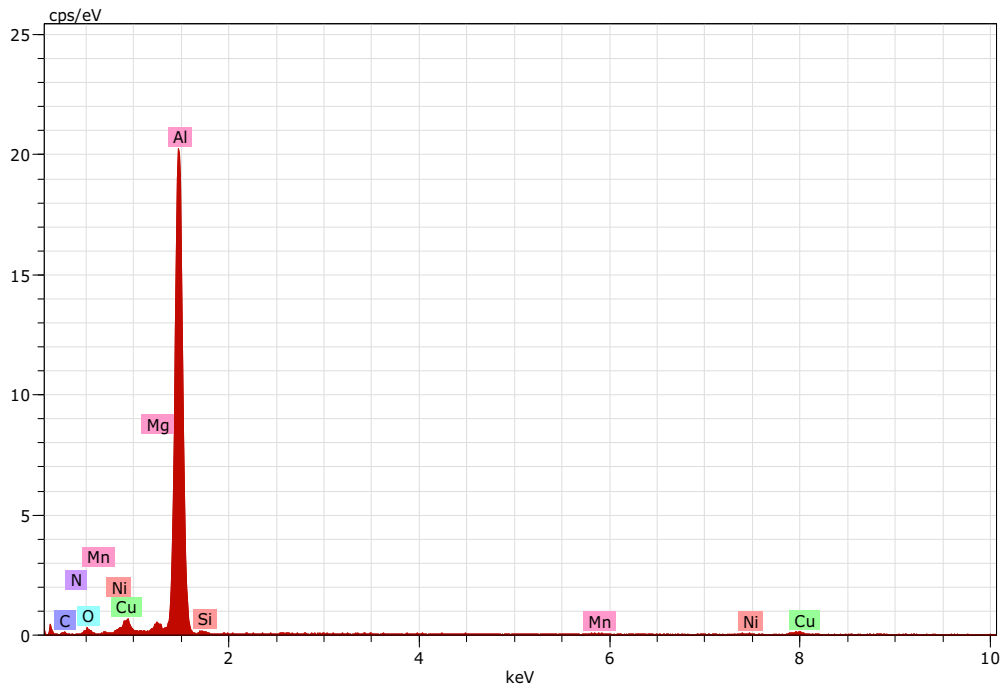
lighter plowing action, suffice a lower wear rate of the alloy composites. The adhesive mechanism might dominate as the surface is free from debris that promotes abrasive action via a three-body wear mechanism.⁴⁰

The micrographs in Figure 8b, c, d, e describe the wear surface damage of the alloy composite at higher operating temperatures. It could be observed that surface damage

signs enhanced with operating temperature rise, e.g., Figure 8b shows severe surface damage via secondary patch formations, relatively deeper plowing action, and grooving. Similarly, Figure 8c shows deep pits with burned surfaces that deteriorate the binding forces between ingredients, causing higher wear debris formation that further promotes the abrasive wear mechanism. This also brings surface fatigue and more surface damage. Further, Figure 8d shows



(b1): SEM area form where mapping data has been collected (b2): EDAX mapping of the elements present in ON13 alloy composite

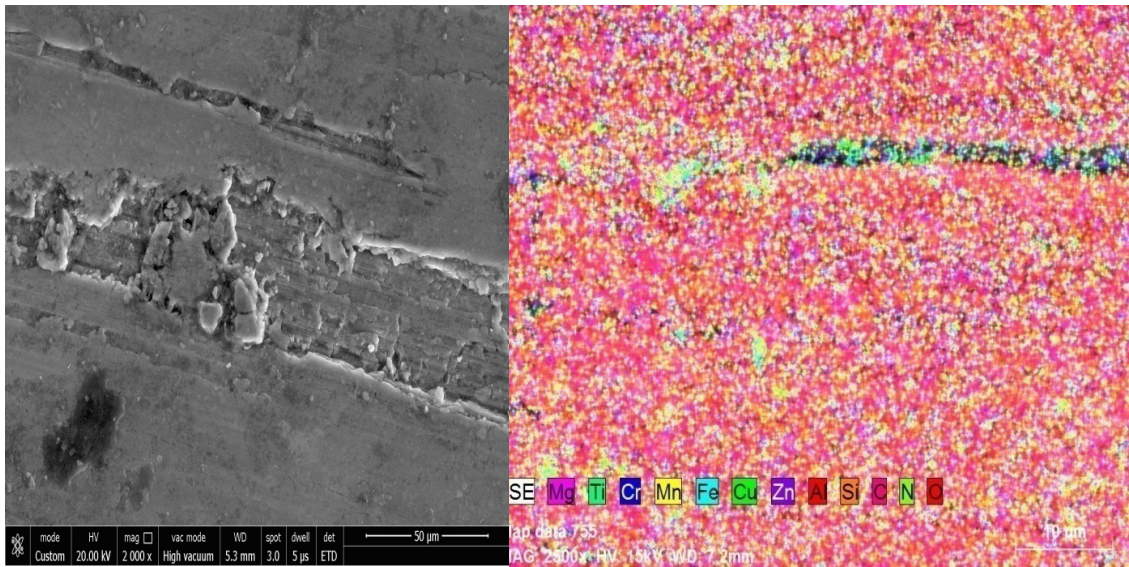


(b3): EDAX spectra showing elements present in ON13 alloy composite (b) ON13 alloy composite

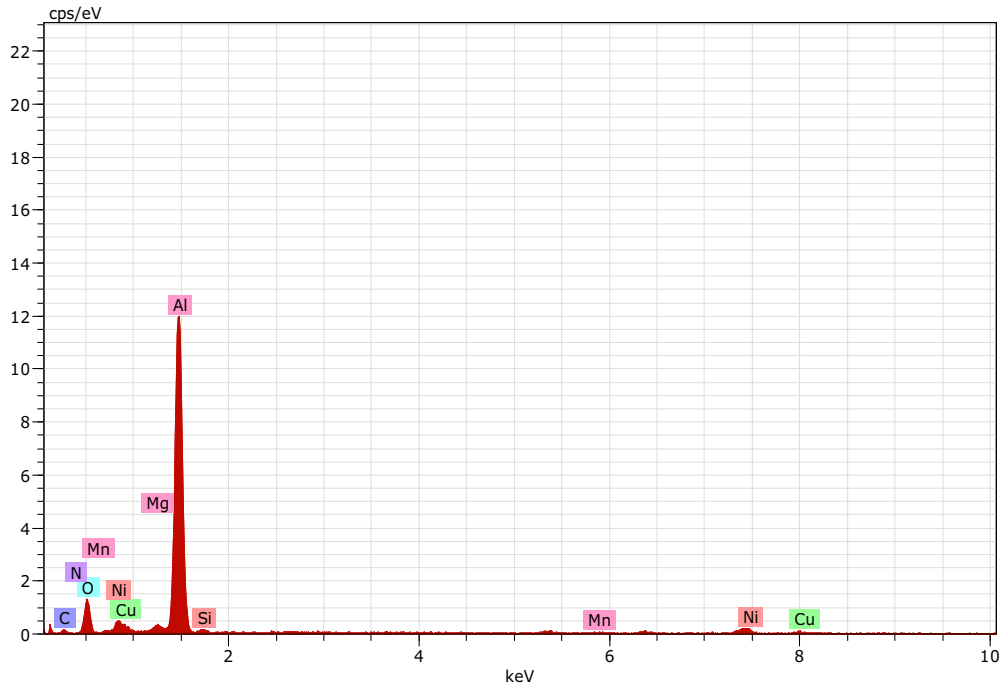
Figure 9. continued

massive surface damage, followed by Figure 8e. Comprehensively, it is seen that as the operating temperature during sliding wear experimentation enhanced, the wear mechanism like surface fatigue, delamination, plowing, grooving, pits, cracking, etc. accelerates and overall brings heavy mass loss from the surfaces. The relative softening of the surface due to temperature improves the

concentration of ceramic particulates in the wear debris as well as in the tribo-layer, which upon destruction, accelerates three-body abrasion and hence further promotes wear rates. At 50 °C, the gain in the thickness of the tribo-layer is expected, which may be due to enhancement in the concentration of detached graphite particulates that probably reduces the rubbing contact area/time of pin-disk



(c1): SEM area form where mapping data has been collected (c2): EDAX mapping of the elements present in ON22 alloy composite



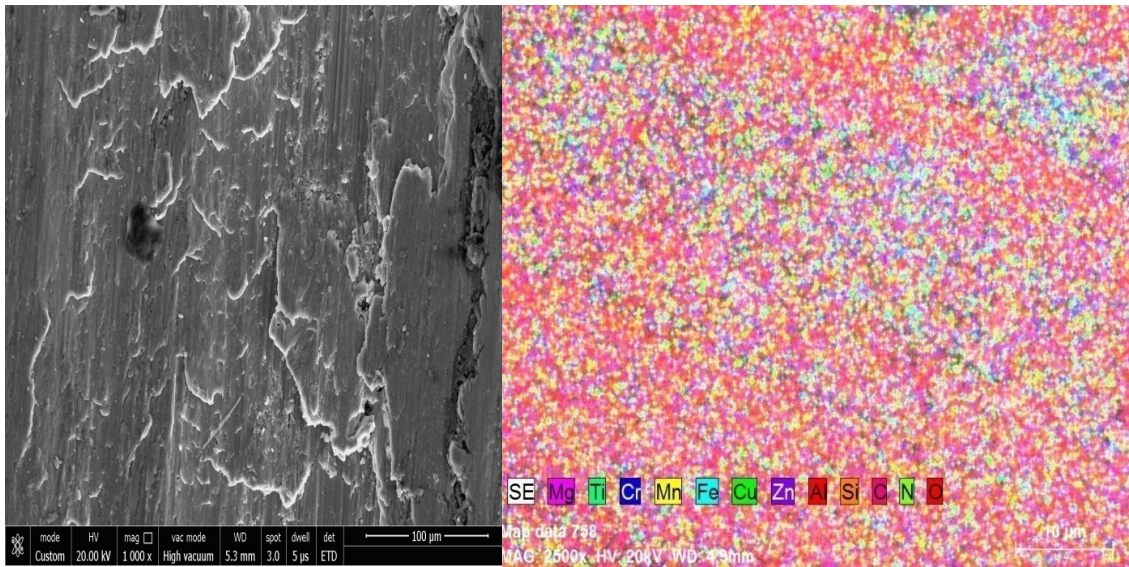
(c3): EDAX spectra showing elements present in ON22 alloy composite
(c) ON22 alloy composite

Figure 9. continued

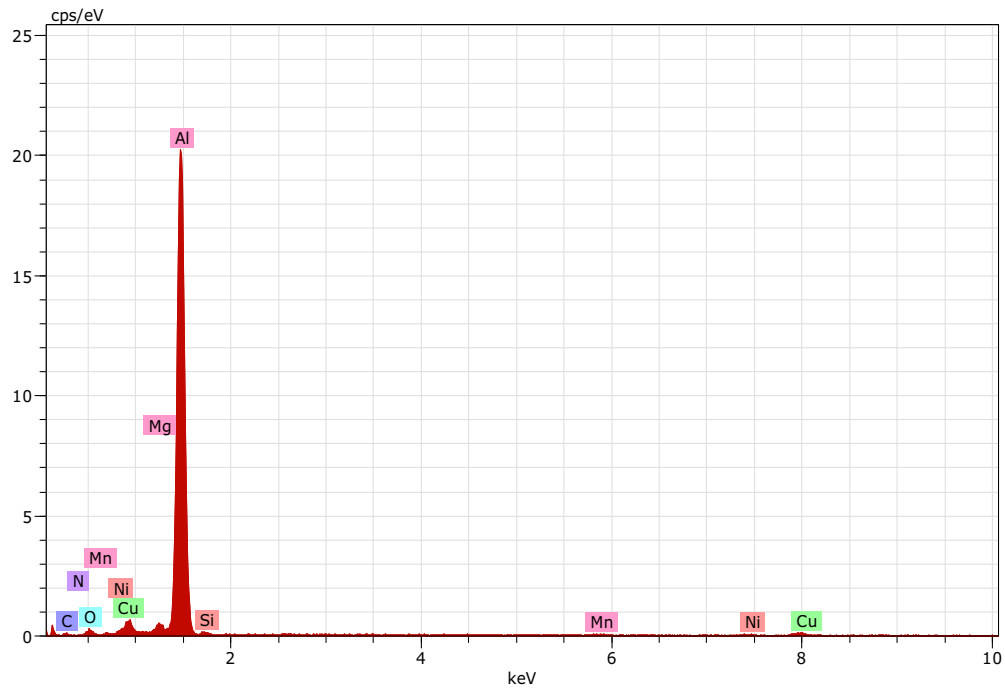
while sliding, consequently resulting in the lower specific wear rate of the alloy composites^{40–47}.

Figure 9 shows the EDAX characteristics of AA2024- $\text{Al}_2\text{O}_3/\text{AlN}$ alloy composites. It indicates different elements present in the materials used for alloy design. The spectra curve indicates the proportion of each element, and

mapping plots indicate their distribution over the surface. The presences of elements like 'Al, C, O, Cu, Mg, Si, Mn, Fe, Zn, N, Ti and Cr' along with reinforcing phases are visible. As the 'Al' element is present in a major amount in alloy and alumina hence showing the largest peak, while the 'C' element presence may be due to graphite content. Similarly, the 'Fe' (iron) element may be due to the



(d1): SEM area form where mapping data has been collected
 (d2): EDAX mapping of the elements present in ON31 alloy composite

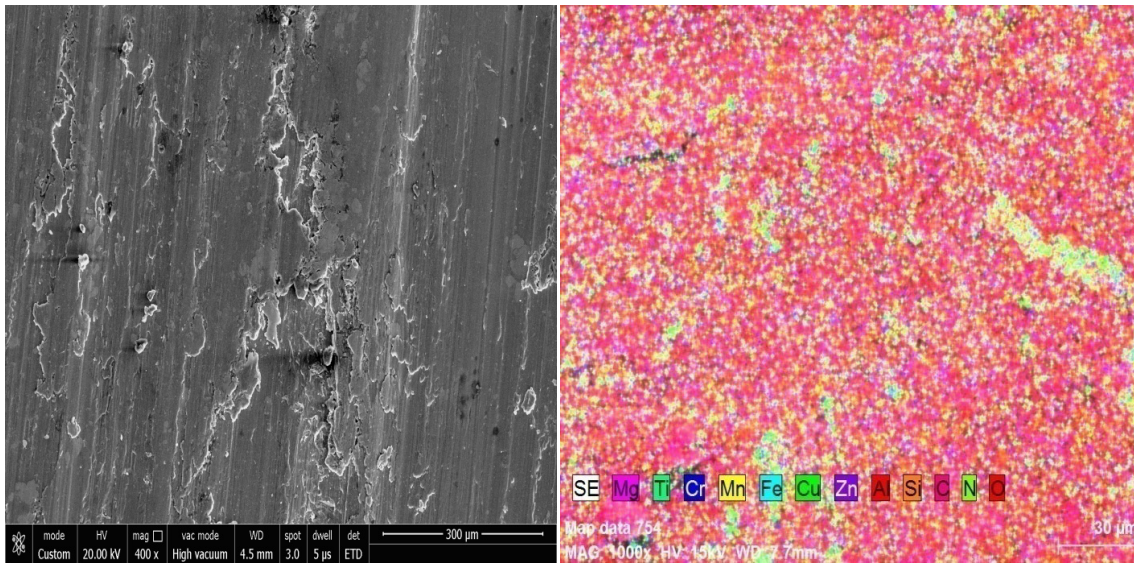


(d3): EDAX spectra showing elements present in ON31 alloy composite
 (d) ON31 alloy composite

Figure 9. continued

counter-surface, which is made of steel; the 'Mg' element presence may be due to alloy together with external addition while fabrication; the 'O' element presence may result due to oxide layer formation during sliding wear experiment was performed in the ambient environment; 'N' element may be due to the presence of AlN particles; rest

traces elements like Cr, Cu, Mn, Ti, Zn, and Pb may be due to the alloy composition. The content of Al increases gradually with 'O' while that of 'N' decreases across the formulation may be due to the complementary presence of ceramic reinforcement in the base alloy matrix.



(e1): SEM area form where mapping data has been collected

(e2): EDAX mapping of the elements present in ON40 alloy composite



(e3): EDAX spectra showing elements present in ON40 alloy composite

(e) ON40 alloy composite

Figure 9. continued

Ranking Analysis Via Preference Selection Index Method

The decision-making tool, namely preference selection index (PSI) method, as discussed in section “[Preference Selection Index Method Procedure](#)”, is applied here on the

decisive matrix (D), having performance criteria listed in Table 9.

The step-wise implementation of the algorithm is as follows:

Step 1: Formulation of the decision problem: The decision goal, performance criteria, and alternatives/formulations of the research work are represented in Figure 10.

Step 2: Determining decision matrix: All the five alternatives (i.e., composite samples) and identified performance criteria are precisely tabulated in the decision matrix form (say matrix D of 5×7 order). Formulated decision matrix is shown in Table 10.

Step 3-5: In the next steps, computation of normalized matrix, preference variation value (PV_j), and overall preference value (ψ_j) need to perform. The calculations are shown in Table 11.

The $\sum \psi_j$ comes out to be equal to 1. The summation of the overall preference value for all criteria must be unity, i.e., $\sum \psi_j = 1$, for consistency.

Step 6-7: In the last steps, preference selection index (I_i) need to be computed, and based upon the score, materials alternatives are ranked in descending order. The ranking order is shown in Table 12.

Table 9. Illustrations of Performance Criteria ²²

Sr. no.	Performance criteria	Preference
PC-1 (TS)	Tensile strength (MPa)	Maximum
PC-2 (FS)	Flexural strength (MPa)	Maximum
PC-3 (IS)	Impact strength (MPa)	Maximum
PC-4 (SWR)	Specific wear rate (mm ³ /Nm)	Minimum
PC-5 (D)	Density (g/cc)	Minimum
PC-6 (VC)	Void content (%)	Minimum
PC-7 (H)	Hardness (HRB)	Maximum

The consistent PSI ranking analysis of performance data was in line with our subjective analysis, i.e., ON22 > ON13 > ON31 > ON04 > ON40. It inferred that (i) the formulations having an equal proportion of Al₂O₃ and AlN ceramic reinforcement presence in AA2024 alloy composites shows the highest ranking, hence subsequently prescribed for tribological applications, (ii) formulations having an unequal amount of either Al₂O₃ and AlN ceramic reinforcement show next level ranking order, where alumina presence proves more promising than AlN reinforcement in the alloy composites; (iii) formulations having either presence of Al₂O₃ or AlN ceramic reinforcement shows lowest ranking order, hence proves least effective. The presence of AlN reinforcement proves more effective than Al₂O₃ reinforcement; and (iv) the study proves that MCDM methods (like PSI) could aid engineers and scientists in material selection and ranking whenever the performance criteria are finite and of conflicting nature.

Conclusions

In this research work, AA2024-Al₂O₃/AlN alloy composites were designed, fabricated, and analyzed for their density, mechanical, and tribological behavior (steady-state sliding wear analysis), adopting ASTM standards. The significant findings are:

1. The densities of the investigated alloy composites remain within 2.539-2.546 g/cc and follow the order ON22 > ON13 > ON31 > ON40 > ON04.
2. The voids fraction remains within the 0.5-9.3 % range and follows the order ON40 > ON04 > ON31 > ON13 > ON22.
3. The Rockwell hardness (HRB) magnitude of the alloy composites increases gradually across the formulation, owing to the mutual effect of ceramic reinforcement in the base alloy matrix.

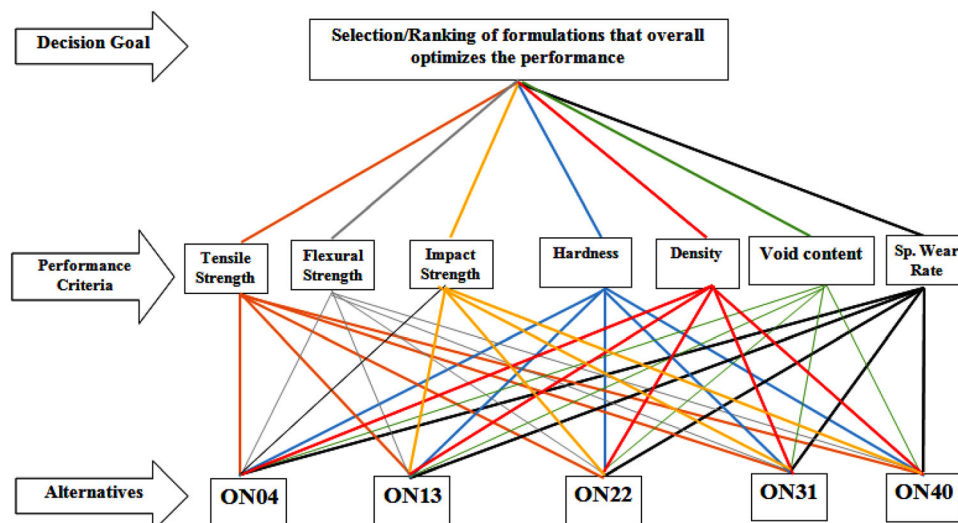


Figure 10. The hierarchy structure of the present investigated.

Table 10. Formulate Decision Matrix (D)

Alternatives (A _i)\ performance criteria (PC _j)	PC-1 (TS)	PC-2 (FS)	PC-3 (IS)	PC-4 (SWR) (× 10 ⁻⁴)	PC-5 (D)	PC-6 (VC)	PC-7 (H)
ON04	206.00	258.48	54.00	1.994	2.55	8.50	71.60
ON13	245.00	272.91	80.00	1.529	2.61	6.60	72.60
ON22	265.00	364.03	170.00	1.384	2.78	0.50	78.20
ON31	213.00	296.98	66.00	1.726	2.56	8.30	79.00
ON40	190.00	267.99	48.00	2.347	2.54	9.30	85.40
Max(X _j)/Min(X _j)	265.00	364.03	170.00	1.38	2.54	0.50	85.40

Table 11. Normalized Decision Matrix, Preference Variation Value (PV_j), and Overall Preference Value (Ψ_j)

Alternatives (A _i)\ Performance Criteria (PC _j)	PC-1 (TS)	PC-2 (FS)	PC-3 (IS)	PC-4 (SWR)	PC-5 (D)	PC-6 (VC)	PC-7 (H)
ON04	0.005	0.009	0.030	0.011	0.000	0.036	0.005
ON13	0.006	0.003	0.000	0.011	0.000	0.030	0.003
ON22	0.024	0.039	0.258	0.041	0.004	0.563	0.000
ON31	0.002	0.000	0.011	0.000	0.000	0.036	0.000
ON40	0.016	0.004	0.044	0.043	0.001	0.038	0.009
SUM(PV _j)	0.053	0.055	0.344	0.106	0.005	0.704	0.017
Φ _j	0.947	0.945	0.656	0.894	0.995	0.296	0.983
Ψ _j	0.166	0.165	0.115	0.156	0.174	0.052	0.172

Table 12. Ranking Order of Materials

Ranking	Materials alternatives (A _i)	Preference selection index (I _i)
1	ON22	0.971
2	ON13	0.792
3	ON31	0.773
4	ON04	0.714
5	ON40	0.712

- The impact strength characteristic of the alloy composite follows the order: ON22 (170 J) > ON13 (80 J) > ON31 (66 J) > ON04 (54 J) > ON40 (48 J).
- The tensile strength follows the order: ON22 (265 MPa) > ON13 (245 MPa) > ON31 (213 MPa) > ON04 (206 MPa) > ON40 (190 MPa).
- The flexural strength follows the order: ON22 (364 MPa) > ON31 (297 MPa) > ON13 (272.9 MPa) > ON40 (267.99 MPa) > ON04 (258.48 MPa).
- The mean S/N ratio for SWR was found to be 76.47 dB. The ranking orders of the significance of input operating factors are Environment temperature > normal load > Sliding velocity > Reinforcement content > Sliding distance. The results of the Taguchi design-of-experiment are

in-tune with that of steady-state experimental results.

- The surface morphology studies reveal the wear mechanisms responsible for surface damage of the investigated alloy composites, and EDAX characteristics indicate different elements present in the materials used for alloy design.
- The consistent PSI ranking analysis of performance data was in line with our subjective analysis, i.e., ON22 > ON13 > ON31 > ON04 > ON40. Hence, MCDM methods (like PSI) could aid the engineer's scientist in material selection and ranking whenever the performance criteria are finite and conflicting.

Acknowledgements

The authors express their sincere gratitude to the Department of Mechanical Engineering of Malaviya National Institute of Technology, Jaipur-302017, Rajasthan, INDIA, for their all kinds of financial as well as other miscellaneous infrastructural support. The authors also acknowledge the aid and facilities provided by the Advanced Research Lab for Tribology and Material Research Centre of the Institute for experimentation and characterization work.

Conflict of interest The author(s) declared no potential conflicts of interest concerning this article's research, authorship, and publication.

REFERENCES

1. M. Kumar, A. Kumar, Sliding wear performance of graphite reinforced AA6061 alloy composites for rotor drum/disk application. *Mater. Today Proc.* **27**, 1972–1976 (2019). <https://doi.org/10.1016/j.matpr.2019.09.042>
2. M. Bai, Q. Xue, Q. Ge, Wear of 2024 Al-Mo-SiC composites under lubrication. *Wear* **195**, 100–105 (1996). [https://doi.org/10.1016/0043-1648\(95\)06808-2](https://doi.org/10.1016/0043-1648(95)06808-2)
3. K.N. Mathan, K.S. Senthil, L.A. Kumaraswamidhas, Aerospace application on Al 2618 with reinforced – Si₃N₄, AlN and ZrB₂ in-situ composites. *J. Alloys Compd.* **672**, 238–250 (2016). <https://doi.org/10.1016/j.jallcom.2016.02.155>
4. A. Baradeswaran, A. Elayaperumal, I.R. Franklin, A statistical analysis of optimization of wear behaviour of Al- Al₂O₃ composites using taguchi technique. *Procedia Eng.* **64**, 973–982 (2013). <https://doi.org/10.1016/j.proeng.2013.09.174>
5. B.C. Kandpal, J. Kumar, H. Singh, Fabrication and characterisation of Al₂O₃/aluminium alloy 6061 composites fabricated by Stir casting. *Mater. Today Proc.* **4**, 2783–2792 (2017). <https://doi.org/10.1016/j.matpr.2017.02.157>
6. S.J. Hong, H.M. Kim, D. Huh et al., Effect of clustering on the mechanical properties of SiC particulate-reinforced aluminum alloy 2024 metal matrix composites. *Mater. Sci. Eng. A* **347**, 198–204 (2003). [https://doi.org/10.1016/S0921-5093\(02\)00593-2](https://doi.org/10.1016/S0921-5093(02)00593-2)
7. G.Q. Chen, W.S. Yang, K. Ma et al., Aging and thermal expansion behavior of Si₃N₄/2024Al composite fabricated by pressure infiltration method. *Trans. Nonferrous Met. Soc. China* **21**, s262–s273 (2011). [https://doi.org/10.1016/S1003-6326\(11\)61589-6](https://doi.org/10.1016/S1003-6326(11)61589-6)
8. R. Abhijith, T.M. Harish, Fabrication analysis of aluminium (Al-2024) and tungsten carbide (WC) metal matrix composite by in-situ method. *Int J Eng Res* **V5**, 400–407 (2016). <https://doi.org/10.17577/ijertv5is080332>
9. S. Pournaderi, F. Akhlaghi, Wear behaviour of Al6061-Al₂O₃ composites produced by in-situ powder metallurgy (IPM). *Powder Technol.* **313**, 184–190 (2017). <https://doi.org/10.1016/j.powtec.2017.03.019>
10. F. Akhlaghi, A. Zare-Bidaki, Influence of graphite content on the dry sliding and oil impregnated sliding wear behavior of Al 2024-graphite composites produced by in situ powder metallurgy method. *Wear* **266**, 37–45 (2009). <https://doi.org/10.1016/j.wear.2008.05.013>
11. N. Hosseini, F. Karimzadeh, M.H. Abbasi, M.H. Enayati, A comparative study on the wear properties of coarse-grained Al6061 alloy and nanostructured Al6061-Al₂O₃ composites. *Tribol Int* **54**, 58–67 (2012). <https://doi.org/10.1016/j.triboint.2012.04.020>
12. R.S.J. David, I. Dinaharan, P.S. Vibin, P.M. Mashini, Microstructure and mechanical characterization of in situ synthesized AA6061/(TiB₂+Al₂O₃) hybrid aluminum matrix composites. *J. Alloys Compd.* **740**, 529–535 (2018). <https://doi.org/10.1016/j.jallcom.2018.01.016>
13. G. Jacob, V.G. Ghica, M. Buzatu et al., Studies on wear rate and micro-hardness of the Al/Al₂O₃/Gr hybrid composites produced via powder metallurgy. *Compos. Part B Eng.* **69**, 603–611 (2015). <https://doi.org/10.1016/j.compositesb.2014.07.008>
14. P. Sharma, S. Sharma, D. Khanduja, Production and some properties of Si₃N₄ reinforced aluminium alloy composites. *J. Asian Ceram. Soc.* **3**, 352–359 (2015). <https://doi.org/10.1016/j.jascer.2015.07.002>
15. K. Umanath, K. Palanikumar, S.T. Selvamani, Analysis of dry sliding wear behaviour of Al6061/SiC/ Al₂O₃ hybrid metal matrix composites. *Compos. Part B Eng.* **53**, 159–168 (2013). <https://doi.org/10.1016/j.compositesb.2013.04.051>
16. A. Devaraju, A. Kumar, B. Kotiveerachari, Influence of addition of Grp/Al₂O₃p with SiCp on wear properties of aluminum alloy 6061–T6 hybrid composites via friction stir processing. *Trans. Nonferrous Met. Soc. China* **23**, 1275–1280 (2013). [https://doi.org/10.1016/S1003-6326\(13\)62593-5](https://doi.org/10.1016/S1003-6326(13)62593-5)
17. S. Dharmalingam, R. Subramanian, V.K. Somasundara, B. Anandavel, Optimization of tribological properties in aluminum hybrid metal matrix composites using gray-taguchi method. *J Mater Eng Perform* **20**, 1457–1466 (2011). <https://doi.org/10.1007/s11665-010-9800-4>
18. M. Kok, Abrasive wear of Al₂O₃ particle reinforced 2024 aluminium alloy composites fabricated by vortex method. *Compos. Part A Appl. Sci. Manuf.* **37**, 457–464 (2006). <https://doi.org/10.1016/j.compositesa.2005.05.038>
19. I. Ozdemir, S. Muecklich, H. Podlesak, B. Wielage, Thixoforming of AA 2017 aluminum alloy composites. *J. Mater. Process Technol.* **211**, 1260–1267 (2011). <https://doi.org/10.1016/j.jmatprotec.2011.02.008>
20. S. Bhaskar, M. Kumar, A. Patnaik, Silicon carbide ceramic particulate reinforced AA2024 alloy composite - part I: evaluation of mechanical and sliding tribology performance. *SILICON* **12**, 843–865 (2020). <https://doi.org/10.1007/s12633-019-00181-x>
21. S. Bhaskar, M. Kumar, A. Patnaik, Microstructure, thermal, thermo-mechanical and fracture analyses of hybrid AA2024-SiC alloy composites. *Trans. Indian Inst. Met.* **73**, 181–190 (2020). <https://doi.org/10.1007/s12666-019-01819-5>
22. S. Bhaskar, M. Kumar, A. Patnaik, Application of hybrid AHP-TOPSIS technique in analyzing material performance of silicon carbide ceramic particulate reinforced AA2024 alloy composite. *SILICON* **12**,

- 1075–1084 (2020). <https://doi.org/10.1007/s12633-019-00211-8>
23. A. Patnaik, P. Kumar, S. Biswas, M. Kumar, Investigations on micro-mechanical and thermal characteristics of glass fiber reinforced epoxy based binary composite structure using finite element method. *Comput. Mater. Sci.* **62**, 142–151 (2012). <https://doi.org/10.1016/j.commatsci.2012.05.020>
 24. A. Kumar, A. Patnaik, I.K. Bhat, Effect of titanium metal powder on thermo- mechanical and sliding wear behavior of Al7075/Ti alloy composites for gear application. *Mater. Today Proc.* **5**, 16919–16927 (2018). <https://doi.org/10.1016/j.matpr.2018.04.095>
 25. A. Kumar, A. Patnaik, I.K. Bhat, Tribology analysis of cobalt particulate filled Al 7075 alloy for gear materials: a comparative study. *SILICON* **11**, 1295–1311 (2018). <https://doi.org/10.1007/s12633-018-9920-2>
 26. D. Petković, M. Madić, M. Radovanović, V. Gečevska, Application of the performance selection index method for solving machining mcdm problems. *Facta Univ. Ser. Mech. Eng.* **15**, 97 (2017). <https://doi.org/10.22190/FUME151120001P>
 27. R. Attri, S. Grover, Application of preference selection index method for decision making over the design stage of production system life cycle. *J. King Saud Univ. – Eng. Sci.* **27**, 207–216 (2015). <https://doi.org/10.1016/j.jksues.2013.06.003>
 28. K. Jha, S. Chamoli, Y.K. Tyagi, H.O. Maurya, Characterization of biodegradable composites and application of preference selection index for deciding optimum phase combination. *Mater. Today Proc.* **5**, 3353–3360 (2018). <https://doi.org/10.1016/j.matpr.2017.11.579>
 29. R. Khorshidi, A. Hassani, Comparative analysis between TOPSIS and PSI methods of materials selection to achieve a desirable combination of strength and workability in Al/SiC composite. *Mater. Des.* **52**, 999–1010 (2013). <https://doi.org/10.1016/j.matdes.2013.06.011>
 30. M. Panahi, H. Gitinavard, Evaluating the sustainable mining contractor selection problems: an imprecise last aggregation preference selection index method. *J. Sustain. Min.* **16**, 207–218 (2018). <https://doi.org/10.1016/j.jsm.2017.12.006>
 31. K.T. Mesran, D.S. Ronda, T.W. Fince, Determination of education scholarship recipients using preference selection index. *Sci. Technol.* **3**, 230–234 (2017)
 32. S.Y. Jian, S.J. Tao, X.R. Huang, Preference selection index method for machine selection in a flexible manufacturing cell. *Adv. Mater. Res.* **1078**, 290–293 (2014). <https://doi.org/10.4028/www.scientific.net/AMR.1078.290>
 33. M. Rahimian, N. Ehsani, N. Parvin, H.R. Baharvandi, The effect of particle size, sintering temperature and sintering time on the properties of Al-Al₂O₃ composites, made by powder metallurgy. *J. Mater. Process Technol.* **209**, 5387–5393 (2009). <https://doi.org/10.1016/j.jmatprotec.2009.04.007>
 34. A. Mazahery, M.O. Shabani, Microstructural and abrasive wear properties of SiC reinforced aluminum-based composite produced by compocasting. *Trans. Nonferrous Met. Soc. China* **23**, 1905–1914 (2013). [https://doi.org/10.1016/S1003-6326\(13\)62676-X](https://doi.org/10.1016/S1003-6326(13)62676-X)
 35. K.S. Santhosh, M. Devaiah, B.V. Seshu, T. Rajasekharan, Mechanical properties of SiC p /Al₂O₃ ceramic matrix composites prepared by directed oxidation of an aluminum alloy. *Ceram. Int.* **38**, 1139–1147 (2012). <https://doi.org/10.1016/j.ceramint.2011.08.042>
 36. B.M. Mahendra, K.P. Arulshri, N. Iyandurai, Evaluation of mechanical properties of Aluminium alloy 2024 reinforced with silicon carbide and fly ash hybrid metal matrix composites. *Am. J. Appl. Sci.* **10**, 219–229 (2013). <https://doi.org/10.3844/ajassp.2013.219.229>
 37. S. Wilson, A.T. Alpas, Effect of temperature on the sliding wear performance of Al alloys and Al matrix composites. *Wear* **196**, 270–278 (1996). [https://doi.org/10.1016/0043-1648\(96\)06923-2](https://doi.org/10.1016/0043-1648(96)06923-2)
 38. P. Ravindran, K. Manisekar, P. Rathika, P. Narayanasamy, Tribological properties of powder metallurgy - Processed aluminium self lubricating hybrid composites with SiC additions. *Mater. Des.* **45**, 561–570 (2013). <https://doi.org/10.1016/j.matdes.2012.09.015>
 39. B.A. Kumar, Murugan n, Dinaharan I, Dry sliding wear behavior of stir cast AA6061-T6/AlNp composite. *Trans. Nonferrous Met. Soc. China* **24**, 2785–2795 (2014). [https://doi.org/10.1016/S1003-6326\(14\)63410-5](https://doi.org/10.1016/S1003-6326(14)63410-5)
 40. S. Mahdavi, F. Akhlaghi, Effect of the graphite content on the tribological behavior of Al/Gr and Al/30SiC/Gr composites processed by in situ powder metallurgy (IPM) method. *Tribol. Lett.* **44**, 1–12 (2011). <https://doi.org/10.1007/s11249-011-9818-2>
 41. S. Gangwar, A. Patnaik, I.K. Bhat, Tribological and thermomechanical analysis of CaO (quicklime) particulates filled ZA-27 alloy composites for bearing application. *Proc. Inst. Mech. Eng. Part L J. Mater. Des. Appl.* **232**, 20–34 (2018). <https://doi.org/10.1177/1464420715609196>
 42. H.Y. Chu, J.F. Lin, Experimental analysis of the tribological behavior of electroless nickel-coated graphite particles in aluminum matrix composites under reciprocating motion. *Wear* **239**, 126–142 (2000). [https://doi.org/10.1016/S0043-1648\(00\)00316-1](https://doi.org/10.1016/S0043-1648(00)00316-1)
 43. D. Lu, M. Gu, Z. Shi, Materials transfer and formation of mechanically mixed layer in dry sliding wear of metal matrix composites against steel. *Tribol. Lett.* **6**, 57–61 (1999). <https://doi.org/10.1023/A:1019182817316>
 44. Y.H. Chae, S.S. Kim, Sliding wear behavior of ceramic, plasma sprayed on casting aluminum alloy

- against SiC ball. Tribol. Lett. **8**, 35–40 (2000). <https://doi.org/10.1023/A:1019110512715>
45. K.N. Tandon, Z.C. Feng, X.Y. Li, Wear behavior of SiC particulate reinforced aluminum composites sliding against steel balls under dry and lubricated conditions. Tribol. Lett. **6**, 113–122 (1999). <https://doi.org/10.1023/A:1019155505930>
46. A. Kumar, M. Kumar, Fracture toughness and thermal investigations of Al7075: cobalt particulates reinforced alloy composites prepared using high vacuum casting method for gear applications: proposed thermal conductivity and fracture toughness modeling. Inter. J. Metal Casting. (2022). <https://doi.org/10.1007/s40962-022-00901-x>
47. A. Kumar, M. Kumar, Investigations on physical, mechanical and sliding wear assessment of ZA27 -Gr

alloy composites using preference selection Index Method. Inter. J. Metal Casting (2023). <https://doi.org/10.1007/s40962-022-00953-z>

Publisher's Note Springer Nature remains neutral with regard to jurisdictional claims in published maps and institutional affiliations.

Springer Nature or its licensor (e.g. a society or other partner) holds exclusive rights to this article under a publishing agreement with the author(s) or other rightsholder(s); author self-archiving of the accepted manuscript version of this article is solely governed by the terms of such publishing agreement and applicable law.